International Journal of Astrobiology 8 (2): 81–94 (2009) Printed in the United Kingdom
doi:10.1017/S1473550409004406

The Earth as an extrasolar planet: the vegetation spectral signature today and during the last Quaternary climatic extrema

Luc Arnold[1], François-Marie Bréon[2] and Simon Brewer[3]

[1]*Observatoire de Haute Provence CNRS INSU, 04870 Saint-Michel-l'Observatoire, France*
e-mail: Luc.Arnold@oamp.fr
[2]*CEA-DSM-LSCE, 91191 Gif-sur-Yvette, France*
[3]*CEREGE, BP 80, 13545 Aix-en-Provence Cedex 04, France*

Abstract: The so-called vegetation red-edge (VRE), a sharp increase in the reflectance around 700 nm, is a characteristic of vegetation spectra, and can therefore be used as a biomarker if it can be detected in an unresolved extrasolar Earth-like planet integrated reflectance spectrum. Here, we investigate the potential for the detection of vegetation spectra during the last Quaternary climatic extrema, the Last Glacial Maximum (LGM) and the Holocene optimum, for which past climatic simulations have been made. By testing the VRE detectability during these extrema, when Earth's climate and biomes maps were different from today, we are able to test the vegetation detectability on a terrestrial planet different from our modern Earth. Data from the Biome3.5 model have been associated to visible Global Ozone Monitoring Experiment (GOME) spectra for each biome and cloud cover to derive Earth's integrated spectra for given Earth phases and observer positions. The VRE is then measured. Results show that the vegetation remains detectable during the last climatic extrema. Compared to the current Earth, the Holocene optimum, with a greener Sahara, slightly increases the mean VRE on one hand, while on the other hand, the large ice cap over the northern hemisphere during the LGM decreases vegetation detectability. We finally discuss the detectability of the VRE in the context of recently proposed space missions.

Received 4 September 2008, accepted 31 December 2008, first published online 26 February 2009

Key words: biomarker, biosignature, Earth spectrum, Earth-like planets, extrasolar planets, Holocene optimum, Last Glacial Maximum, modern Earth, vegetation.

Introduction

One of the most challenging goals of the future space missions is to detect life on extrasolar planets. These missions are designed to image a planet as a single dot floating beside its parent star, using high-contrast imaging techniques. Photons from the unresolved planet will feed a low-resolution spectrograph and give the first insights into the planet's chemistry. Recent works suggest that Earth's vegetation is detectable in Earth's integrated spectrum at visible wavelengths (Arnold *et al*. 2002; Woolf *et al*. 2002; Arnold 2008), assuming extraterrestrial plants, if they exist, are similar to Earth's plants. Our green vegetation indeed has a reflectance spectrum showing a sharp increase – the so-called vegetation red-edge (VRE) – around 700 nm (Fig. 1), which could be considered as a possible global biomarker.

A question arising from these results is whether vegetation was also detectable when the (early) Earth looked significantly different than today. In other words, if an Earth-like planet with a climate different from the modern Earth's climate is detected one day, will we be able to detect vegetation on it? To answer this, we investigate the vegetation spectral detectability during the last Quaternary climatic extrema, for which past climate simulations have been made by general circulation models (GCMs). This simulated climate is used as a driver for an equilibrium vegetation model, providing biome maps of the Earth at these epochs.

The Last Glacial Maximum (LGM) occurred about 21 kyr (kilo-years) ago. Temperatures globally of the order of 4 °C colder than today (Braconnot *et al*. 2007) were responsible for a large extent of sea and continental ice sheets, especially in the northern hemisphere. The sea level was also significantly lower (-121 ± 5 m (Fairbanks 1989)), resulting in larger emerged lands.

During the Holocene optimum (6 kyr before present, hereafter kyrBP), Earth's northern hemisphere was ≈ 0.5 °C warmer than today (Braconnot *et al*. 2007). The sea level was rising, although it was still slightly lower than today, because the amount of water released from continental ice was partially compensated by an isostatic response of the continents, i.e., a rise of the continents following the deglaciation of the northern hemisphere. The Sahara was more vegetated than

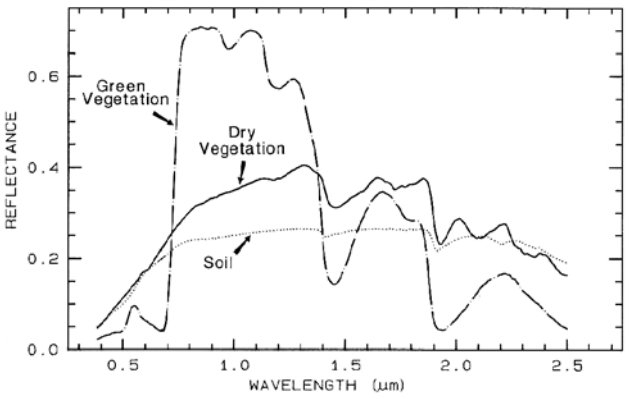

Fig. 1. Reflectance spectra of photosynthetic (green) vegetation, non-photosynthetic (dry) vegetation and soil (from Clark (1999)). The so-called VRE is the green vegetation reflectance strong variation from ≈5% at 670 nm to ≈70% at 800 nm. Note that the spectrum of a non-vegetated soil also shows a higher reflectance in the IR than in the visible.

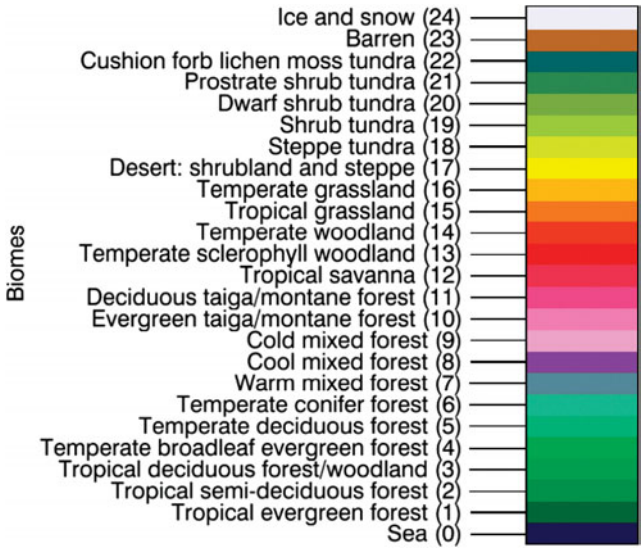

Fig. 2. Map legend and biomes index.

today (Ritchie & Haynes 1987; Bonfils *et al.* 2001), its desertification being the main large-scale change in land cover for the last 6000 years (Claussen *et al.* 1999).

Here, based on a combination of biomes and simulated cloud cover maps for the periods mentioned above, associated with 300–800 nm spectra for each biome and cloud, we build Earth-integrated spectra for given Earth phases and observer positions. The vegetation spectral signature is then extracted from these spectra. The first part of the paper describes the model of the Earth from which we derive global reflectance spectra. The second part of the paper discusses the results. Note that movies showing the rotating Earth and corresponding instantaneous spectrum are available on-line (http://www.obs-hp.fr/~larnold/results/2009_IJAstrobio/VRE.html).

Main inputs for the Earth model

Biomes maps from Biome3.5 model for 0, 6 and 21 kyrBP

The equilibrium terrestrial biosphere model BIOME3 (Haxeltine & Prentice 1996) is a process-based vegetation model simulating biogeography and biogeochemistry. Model inputs consist of monthly climate variables (temperature, precipitation, and sunshine) data, minimum annual temperature and atmospheric CO2 concentration. A coupled hydrological model calculates moisture availability on the basis of a soil texture class. The model simulates the productivity and cover (Leaf Area Index) of a set of plant functional types. The comparative dominance of these types is then used to estimate the dominant biome for a given grid cell. A total of 24 biomes may be simulated, including barren ground and snow/ice cover (Figs. 2 and 3).

The model was run for the three periods of interest: modern, Holocene optimum and LGM Earth (Figs. 2 and 3). For the modern period, gridded climate data on a 0.5° grid was taken from Leemans & Cramer (1991), and atmospheric CO2 concentration was set to a pre-industrial level of 280 ppm. For the two past periods, climate data was obtained from simulations run under the Paleoclimate Modelling Intercomparison Project[1]. We used data from the UK Meteorological Office General Circulation Model (UKMO GCM), run under climatic forcings for these two periods (Hewitt & Mitchell 1996, 1997). The GCM output was downscaled to the same resolution grid as the modern period by calculating anomalies for each past period. The GCM control run value was subtracted from the past value for each GCM grid point, and then these anomalies were added to the modern climatology grid points. Atmospheric CO2 concentration was set to 265 ppm and 180 ppm for the Holocene optimum and LGM respectively.

The results obtained agree well with observational evidence of past vegetation change (Prentice *et al.* 2000). The mid-Holocene is dominated by a greening of the Sahara, and a poleward shift of the high latitude treelines. The LGM is characterized by a large expansion of steppe and grassland vegetation at mid-latitudes, with a near disappearance of temperate forest. There is also the fragmentation of tropical forest and widespread expansion of tundra vegetation at high latitudes. There are, however, some disagreements with the data, for example the expansion of grassland in Australia.

Biome spectra

We used a collection of GOME (Global Ozone Monitoring Experiment) spectra taken on the 18th, 19th and 20th of May 1999, corresponding to springtime and the middle of the greenup period in the northern hemisphere. In May the average Normalized Differential Vegetation Index (NDVI) is just half of its maximum value reached in July[2]. The Sun

[1] Paleoclimate Modelling Intercomparison Project (PMIP), http://pmip.lsce.ipsl.fr/.

[2] http://earthobservatory.nasa.gov/Newsroom/NewImages/Images/PIA04335.gif.

https://doi.org/10.1017/S1473550409004406 Published online by Cambridge University Press

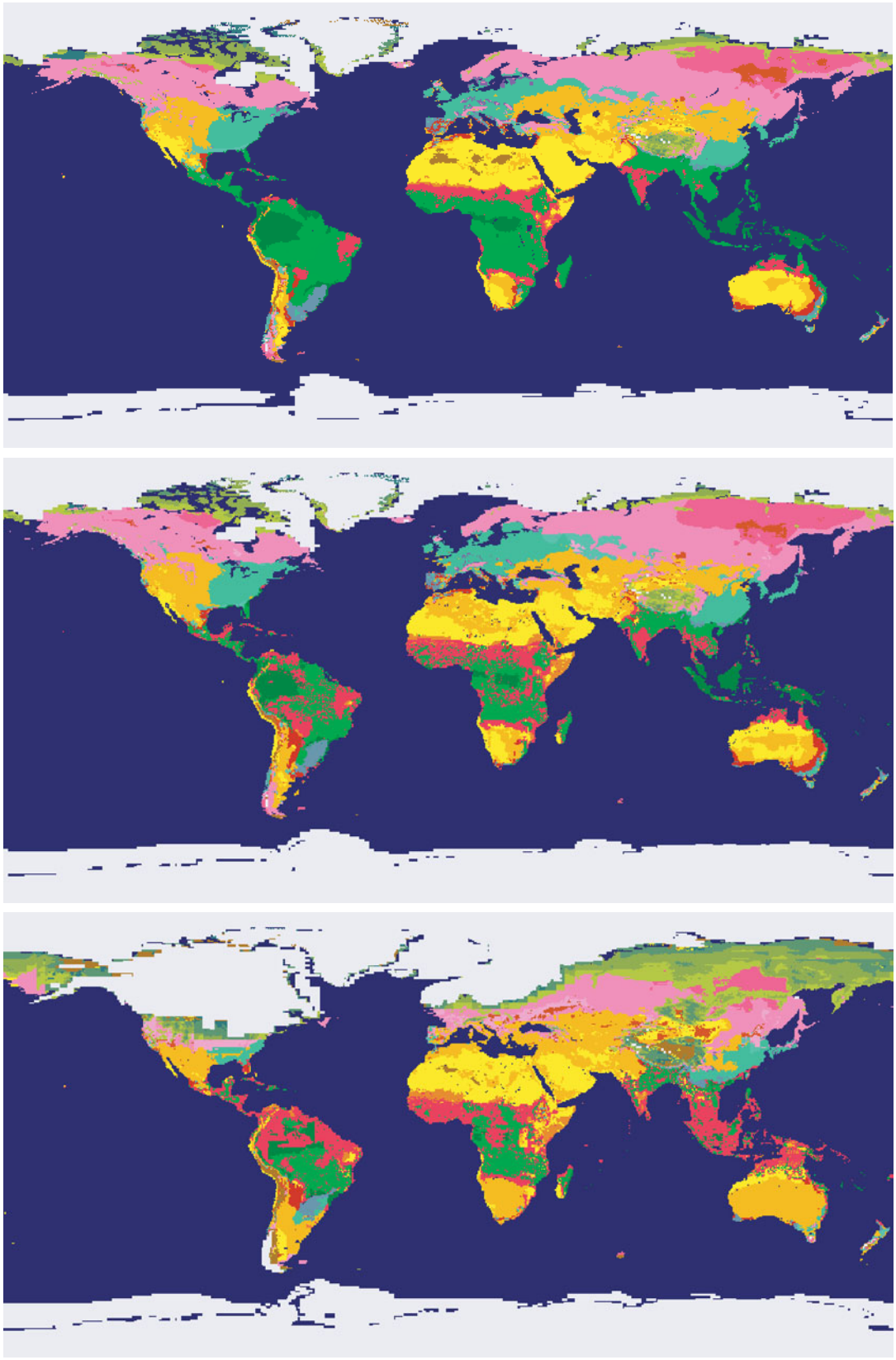

Fig. 3. Maps of biomes today: (top) 6 kyrBP during the Holocene optimum; (middle) 21 kyrBP during the LGM; (bottom) with continental and sea ices. Note that at 6 kyrBP, a large part of the Sahara displayed a temperate grassland biome and almost no barren regions, while today and at 21 kyrBP, it consists of barren and desert (shrubland and steppe) landscapes.

https://doi.org/10.1017/S1473550409004406 Published online by Cambridge University Press

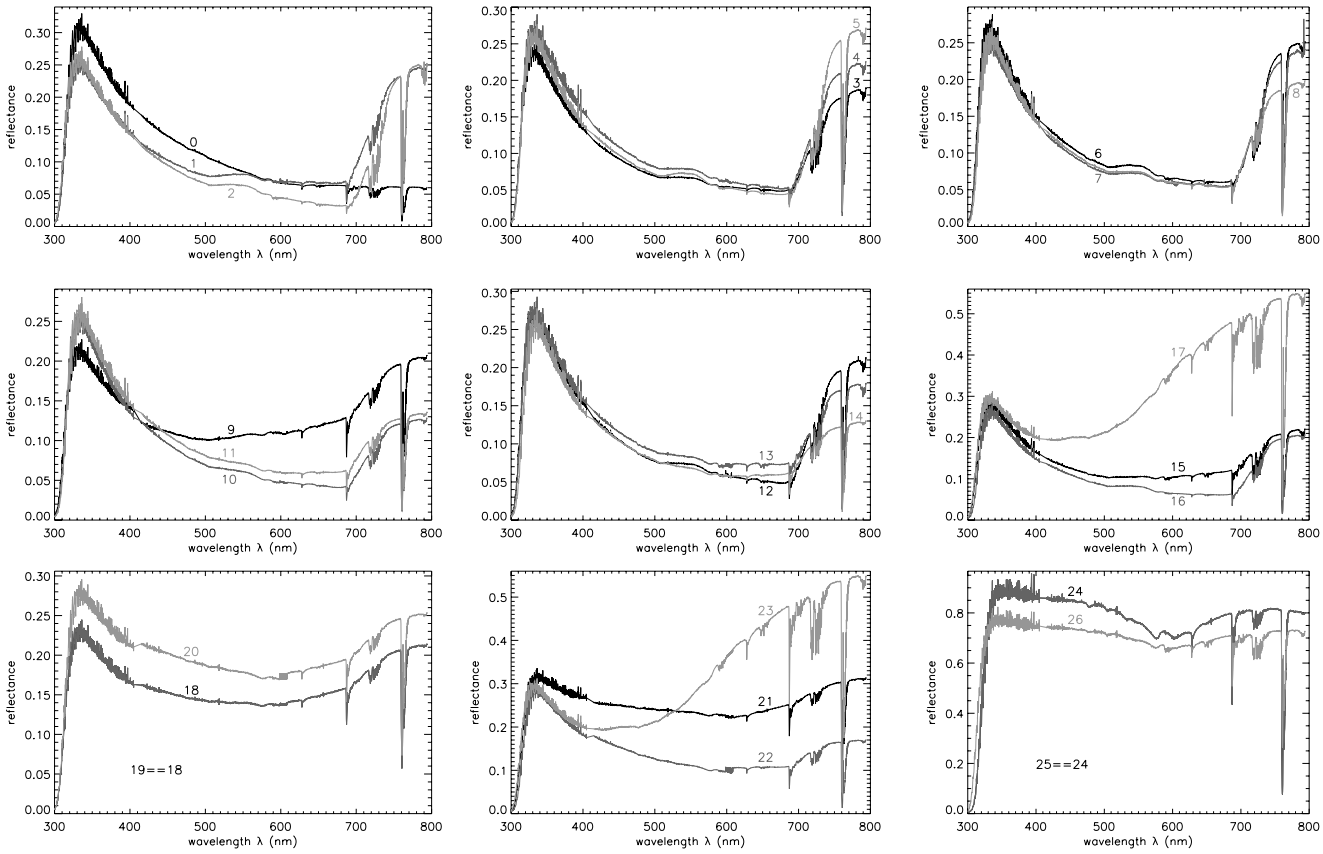

Fig. 4. Biomes spectra measured by GOME on the 18th, 19th and 20th of May 1999. The spectra have been recorded at air-mass (i.e. back and forth path length through the atmosphere) ranging from 2 to 2.6 depending on solar and spacecraft line-of-sight angles. See Fig. 2 for the biome legend. Note that all plots do not have the same vertical scale.

declination is $\approx +19.7^\circ$ for the observing dates in May. It is fall in the southern hemisphere and the polar night is present at latitudes below -70.3°. The GOME spectra are reflectances obtained from the ratio of a given ground pixel radiance R over solar irradiance $I_\odot$,

$$r_\mathrm{b} = \frac{\pi R}{I_\odot \cos\theta_\mathrm{s}}, \tag{1}$$

where θ_s is the solar zenit angle. A reference spectra for each biome r_b is extracted from the GOME data (Fig. 4). In order to find a given biome spectrum with minimal cloud contamination, the algorithm chooses the spectrum with the lowest signal in the interval from 450 to 500 nm, considering that the signal in this spectral range rapidly increases with the presence of clouds. This algorithm fails for three types of surfaces: oceans, snow/ice and cloud. These spectra are chosen 'by hand'.

It must also be noted that this algorithm chooses the most vegetated pixel for a given biome; if a cloudless pixel is a mixture of sand and vegetation, it will be ignored in favour of a pixel with more vegetation, which will display a lowest signal in the spectral interval mentioned. This suggests that the reference pixel (and spectrum) for each biome is probably biased toward the most vegetated pixel of a given biome area.

Lastly, since it is spring in the northern hemisphere and fall in the southern hemisphere, the reference spectrum for the biomes of deciduous species will be preferentially picked up in the 'greener' northern hemisphere. Therefore, our simulations will be more relevant for reconstruction of the northern hemisphere rather than of the southern hemisphere, with a probable overestimate of the vegetation signal if the southern hemisphere is mainly in view.

Cloud cover

Modern cloud cover reflectance from International Satellite Cloud Climatology Project data

To build a realistic Earth spectrum, we need both the cloud cover map and the reflectance map of that cloud cover, r_cc. We used cloud covers from the International Satellite Cloud Climatology Project (ISCCP[3]). We selected only data for the month of May from 1999 to 2004 Vis-infrared (IR) observations, to be consistent with the GOME spectra. Since low, middle and high altitude clouds have different typical optical depth and reflectances, we build the cloud cover reflectance r_cc from the sum of the three different altitude cloud cover maps, cc_L, cc_M and cc_H, weighted by their albedo, a_L, a_M and a_H, respectively 0.69, 0.48 and 0.21 (Manabe & Strickler

[3] http://isccp.giss.nasa.gov/.

https://doi.org/10.1017/S1473550409004406 Published online by Cambridge University Press

Table 1. *Quantitative data about cloud cover normalized reflectance from real data* (*ISCCP*) *and model* (*biome3.5*)

	Modern Earth (ISCCP)	Modern Earth (biome3.5)	Holocene optimum (biome3.5, 6 kyrBP)	LGM (biome3.5, 21 kyrBP)
Mean R_{cc}	0.46	0.40	0.40	0.39
Max R_{cc}	0.86	1.00	1.00	1.00
Min R_{cc}	0.00	0.03	0.03	0.05
$+60^\circ+90^\circ$	0.51	0.50	0.50	0.41
$+40^\circ+60^\circ$	0.53	0.52	0.52	0.58
$-40^\circ+40^\circ$	0.38	0.22	0.22	0.24
$-60^\circ-40^\circ$	0.62	0.81	0.81	0.75

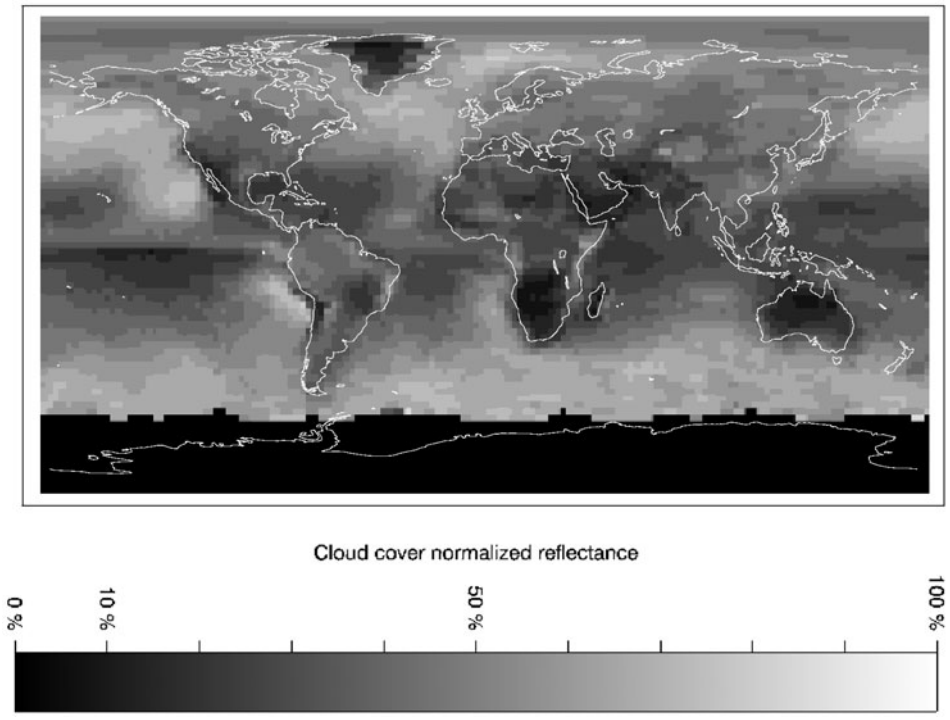

Fig. 5. Normalized reflectance map of the cloud cover estimated from ISCCP data on low, mid and high cloud cover maps and clouds albedo (Manabe & Strickler 1964) for the mean of cloud cover for the month of May for six years from 1999 to 2004. No data are available for Antarctica because this region is always in the night in May. Quantitative data are given in Table 1.

1964), and normalized to the albedo of low altitude clouds a_L, i.e.,

$$r_{cc} = cc_L + \frac{a_M}{a_L} cc_M + \frac{a_H}{a_L} cc_H. \quad (2)$$

The result from this formula is that the three different types of clouds contribute to a given pixel's reflectance proportionally to their cover over that pixel. The formula can also lead to a few pixels with reflectance above 1, which are then simply clipped to 1. The obtained map (Fig. 5 and Table 1) is normalized to the albedo of low clouds for which we have a reference spectrum from the GOME data.

Cloud cover from Biome3.5 model for 0, 6 and 21 kyrBP

Estimates of past changes in cloud cover were taken from the UKMO GCM, as used as input for the Biome3.5 model. The 0 and 6 kyrBP cloud covers are the same (Fig. 6). The simulated cloud cover at 21 kyrBP shows locally overestimated cloud cover in the southern hemisphere, caused by the existence of a wavetrain resulting from the passage of the lower atmospheric circulation over the topography of South America (Fig. 6). The simulated cloud cover output consists of 17 layers of clouds at given pressures from 1000 (ground) to 10 mbar (highest clouds). The model shows that the highest layers, at 30, 20 and 10 mbar, are very high clouds above Antarctica at night, which are therefore not relevant for our study. The remaining 14 layers are quadratically summed into three layers of low, middle and high clouds, according the ISCCP classification versus cloud pressure[4] (i.e., low clouds for pressures from 1000 to 680 mbar, middle clouds from 680 to 440 mbar, and high clouds above 440 mbar). A simple sum of the 14 layers into 3 would mean that the clouds in each layer contribute linearly and cumulatively to the total cloud cover over a given pixel.

[4] http://climate.msrc.sunysb.edu/cpt/isccp-cltypes.gif.

https://doi.org/10.1017/S1473550409004406 Published online by Cambridge University Press

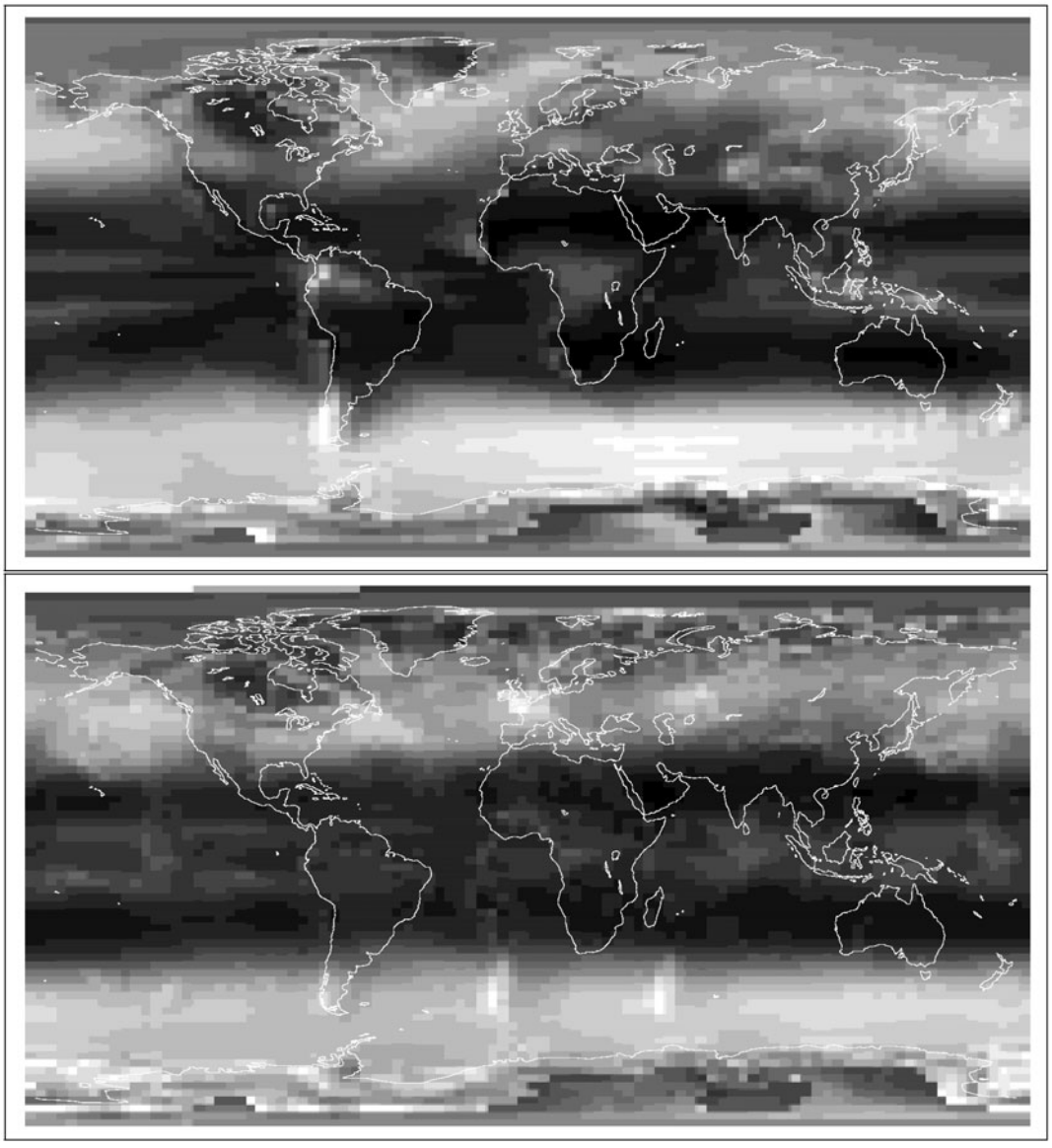

Fig. 6. Normalized reflectance maps of the cloud cover estimated from cloud cover simulated by the UKMO GCM, with the same grey-scale as for Fig. 5, for modern Earth or at 6 kyrBP (top) and 21 kyrBP (bottom). In the 21 kyrBP map, artifacts induced by the existence of a wavetrain resulting from the passage of the lower atmospheric circulation over the topography of South America are visible in the southern hemisphere: The cloud cover is slightly overestimated in the middle of the Atlantic Ocean and at the South of Madagascar Island. Quantitative data are given in Table 1.

This is not realistic and leads to overestimation of cloud cover (many pixels have a cloud cover significantly larger than 100 %). Using a quadratic sum allows the superimposition of layers to be taken into account, leading to much more realistic results when the 0 kyrBP model is compared with real ISCCP data. The cloud reflectance maps are calculated following Eq. (2) as done with the ISCCP data.

Disk-averaged spectra from the model and extraction of the vegetation signal

A two-layer map of the Earth is created with biome and cloud cover for each pixel. For the ocean, two-layers are used too, but the biome is replaced with the sea ice cover. Once this composite map is built, we proceed with an orthographic projection where the central longitude and latitude corresponds to the position chosen for the virtual distant observer. A realistic image of the Earth, i.e., a radiance map, with limb darkening and phase, is finally obtained by multiplying the previous projection by a mask of a white Lambertian sphere at the desired phase. We consider indeed a Lambertian Earth, i.e., all biomes, ocean and clouds have an isotropic reflectance. Thus no specular reflection on the ocean surface is taken into account. Specular reflection has indeed an albedo of 0.02, moreover attenuated by lands and clouds (Bréon & Henriot 2006). We estimate from Bréon & Henriot (2006) that specular reflection would increase the overall Earth albedo by ≈ 0.01 and therefore has a negligible quantitative impact.

https://doi.org/10.1017/S1473550409004406 Published online by Cambridge University Press

Table 2. *24 h-averaged disk-averaged VRE (%) and apparent albedo A_v measured from our Earth model during springtime for different Earth phases and observer's positions. The angle ϕ is the orbital phase: $\phi = 0^\circ$ is for the Western maximum elongation, $\phi = 90^\circ$ for superior conjunction, $\phi = 180^\circ$ for the Eastern elongation and $\phi = 270^\circ$ for inferior conjunction (See Fig. 7, 8 and 9 for detailed results and Earth's scenes)*

	Epoch and data			
	Modern 0 kyrBP ISCCP	Modern 0 kyrBP Biome3.5	Holocene optimum 6 kyrBP Biome3.5	LGM 21 kyrBP Biome3.5
$i = 45^\circ$, $\phi = 180^\circ$ (eastern elongation, half-Earth)				
$\langle$VRE$\rangle$	4.4	5.1	5.8	3.4
A_v	0.368	0.323	0.320	0.359
$i = 45^\circ$, $\phi = 90^\circ$ (superior conjunction, $\approx$ full Earth)				
$\langle$VRE$\rangle$	4.7	5.7	6.7	4.3
A_v	0.347	0.293	0.290	0.328
$i = 45^\circ$, $\phi = 270^\circ$ (inferior conjunction, crescent Earth)				
$\langle$VRE$\rangle$	2.5	2.4	2.6	0.8
A_v	0.466	0.456	0.455	0.489
$i = 0^\circ$, $\phi = 180^\circ$ (ecliptic north pole view, half-Earth)				
$\langle$VRE$\rangle$	4.3	4.3	4.7	2.0
A_v	0.395	0.370	0.368	0.418
$i = 90^\circ$, $\phi = 180^\circ$ (eastern elongation, half-Earth)				
$\langle$VRE$\rangle$	5.0	7.4	8.4	6.9
A_v	0.312	0.237	0.234	0.255
$i = 135^\circ$, $\phi = 180^\circ$ (eastern elongation, half-Earth)				
$\langle$VRE$\rangle$	4.2	6.7	7.0	7.7
A_v	0.311	0.233	0.232	0.231
$i = 180^\circ$, $\phi = 180^\circ$ (ecliptic south pole view, half-Earth)				
$\langle$VRE$\rangle$	3.9	5.8	5.8	6.7
A_v	0.324	0.255	0.255	0.249

We assume that a Lambertian approximation of biomes reflection, with respect to real anisotropic Bidirectional Reflectance Distribution Function (BRDF), has negligible impact on the global spectrum. Specular reflection of the Sun in the ocean would make the Earth brighter and consequently decrease the relative signal of vegetation. Our model also considers all clouds as optically thick, which, according to ISCCP, means optical thickness of clouds[5] equal to 3.86. We understand that to derive more accurate spectra, our model would probably benefit from radiative transfer calculations, an implementation of the sun glint effect and the BRDFs of all scattering surfaces included in the model (biomes, oceans, clouds).

The global spectrum is computed from the projection of the Earth as described above: the global Earth Reflectance spectrum $ER(\lambda)$ is a linear combination of the spectra of each biome, ocean (ice-free or partly covered by sea ice) and clouds, weighted by their respective number of pixels and integrated radiance in the projected image, a pixel being itself a combination of two or three elements (biome and cloud, or sea, sea ice and cloud). The result is normalized to the flux integrated in the image of a white Lambertian sphere observed with the same phase, giving the result spectrum in terms of apparent albedo A_v (Qiu *et al.* 2003).

We want to measure the height of the VRE embedded in Earth's reflectance $ER(\lambda)$, considered as an example of a large-scale ground-based signature of life. We want to remove all *a priori* known biases, these biases being due to atmospheric molecules of biotic or abiotic origin, or due to known minerals spread over large land surfaces. The VRE is quantitatively approximated by the ratio (Arnold *et al.* 2002; Hamdani *et al.* 2006)

$$\mathrm{VRE} = \frac{r_\mathrm{I} - r_\mathrm{R}}{r_\mathrm{R}}, \tag{3}$$

where r_I and r_R are the near-infrared (NIR) and red reflectances integrated over spectral domains defined on both sides of the Red Edge. This formula gives correct results only if the spectrum has been cleaned from known sources of atmospheric bias, as described above. There are at least three

[5] ISCCP data analysis http://isccp.giss.nasa.gov/climanal1.html.

https://doi.org/10.1017/S1473550409004406 Published online by Cambridge University Press

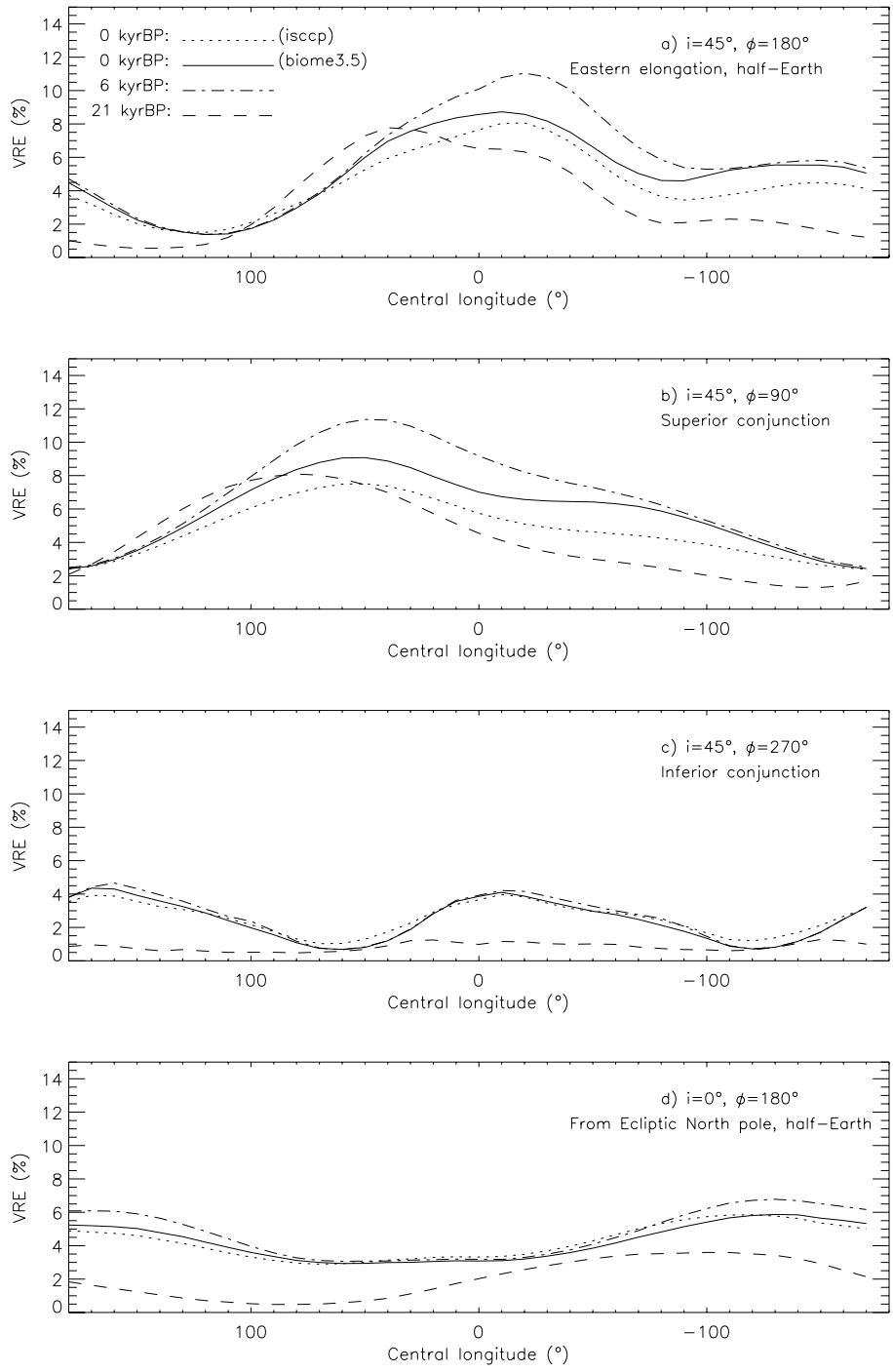

Fig. 7. VRE measured with Biome3.5 data for clouds, ice and biomes, and GOME spectra (and ISCCP for clouds at 0 kyrBP only). The VRE calculated with the ISCCP clouds and the BIOME3.5 model are in correct agreement, although the latter is typically 1 % higher. Central longitude is decreasing, according to the eastward Earth rotation (See Fig. 9 for corresponding Earth's scenes).

sources of bias that can be corrected *a priori* and that have been considered here.

The first is the absorption of atmosphere molecules. Ozone has a weak but wide absorption over the full visible range (the Chappuis band), and absorption is non-zero at the wavelengths of interest for the VRE. The Earth spectrum is thus divided by a reference ozone absorption spectrum, extracted from a GOME spectrum of white clouds and adjusted to the data. Water vapour and oxygen absorptions are also corrected with MODTRAN[6] reference spectra: the band depth of the reference spectra are optimized to minimize the residual of the fit, after which the spectrum is divided by the fit. These two molecules have a lower impact on the VRE

[6] MODTRAN is distributed by Ontar Corporation.

https://doi.org/10.1017/S1473550409004406 Published online by Cambridge University Press

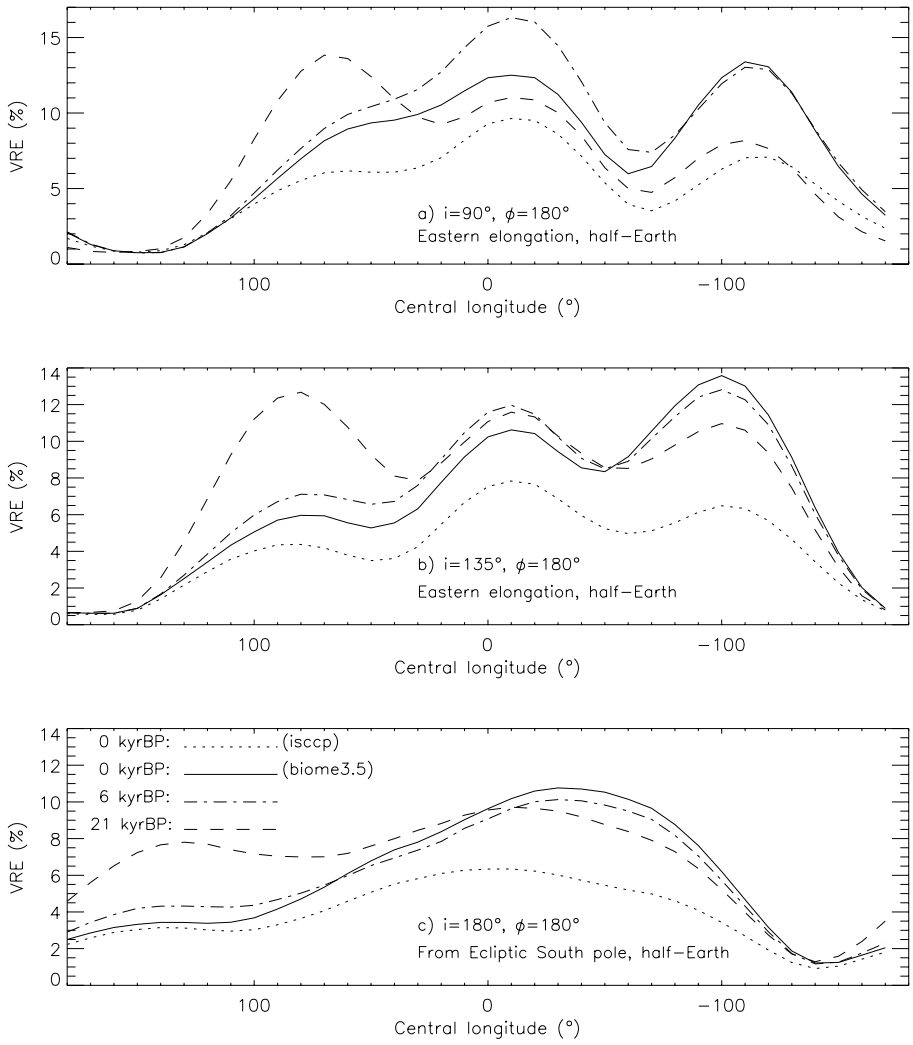

Fig. 8. VRE measured with Biome3.5 for clouds, ice and biomes, and GOME spectra (and ISCCP for clouds at 0 kyrBP only). The VRE calculated with the ISCCP clouds are significantly lower than those calculated from the BIOME3.5 model, probably due to the difference between the corresponding cloud maps for the southern hemisphere as suggested by Table 1. Central longitude is decreasing, according to the eastward Earth rotation (See Fig. 9 for corresponding Earth's scenes).

extraction than ozone because their absorption bands are relatively narrow, moreover the spectral domains over which the VRE is measured can be chosen between H_2O and O_2 absorption bands.

Scattering in the atmosphere is the second source of bias we take into account. Rayleigh and aerosol scattering produce a negative slope in the spectrum in the blue part of the spectrum. We consider here that the aerosol and the Rayleigh contribution to scattering are equal at $\lambda_e = 700$ nm (Léna *et al*. 1996).

The third source of bias we take into account is the spectral signature of deserts that add a smooth positive slope across the visible and NIR domains where the VRE is measured (Arnold *et al*. 2003; Arnold 2008), and the function defined to fit Rayleigh, aerosol and desert biases from 350 to 685 nm is thus written

$$f(\lambda) = \left(A_0 + \frac{A_1}{\lambda^4 + \lambda_e^{2.5}\lambda^{1.5}} + A_2 \times s_d \right) \times s_{O_3}^{A_3}. \quad (4)$$

The spectrum s_d is our model of desert reflectance, extracted from a GOME spectrum taken over the Sahara and corrected for Rayleigh and ozone biases, and s_{O_3} is the spectrum of ozone extracted from a GOME spectrum of white clouds. The $ER(\lambda)$ spectrum is then normalized to the vegetationless model $f(\lambda)$ to measure the VRE using the spectral domains [650:685 nn] and [750:758 nm]. It can be noted here that the correction of H_2O and O_2 is only relevant for the fit function between 580 and 680 nm.

To test the robustness of these bias corrections, we built an Earth model where all pixels of continents were desert, with oceans, clouds, sea and continental ices remaining unchanged. We obtained a mean VRE of 0.1% with a standard deviation of 0.2% after an integration over a full Earth rotation, for an observer seeing mostly the northern hemisphere of a half-phase Earth (inclination $i = 60°$, orbital phase $\phi = 180° -$ eastern elongation). For identical geometrical parameters, the vegetated Earth model gives a VRE of 5.9% (standard deviation of 2.9%) suggesting that the $f(\lambda)$ function

https://doi.org/10.1017/S1473550409004406 Published online by Cambridge University Press

well fits a vegetationless spectrum, i.e., meaning that the biases mentioned above are well corrected to allow the detection and the measurement of VRE values as low as $\approx 1\%$.

Results and discussion

The reconstructed scenes of the Earth, from which the results below are extracted, have been made using a Sun declination of $\delta = +19.7^\circ$, corresponding to the Earth–Sun configuration for May. The Earth phase viewed by the observer is reconstructed for several inclinations i. The angle ϕ is the orbital phase of the Earth viewed from the location of the observer: $\phi = 0^\circ$ is for the Western maximum elongation, $\phi = 90^\circ$ for superior conjunction, $\phi = 180^\circ$ for the Eastern elongation and $\phi = 270^\circ$ for inferior conjunction.

In Table 2, the VRE and albedo values obtained from the model are given for the different periods and illustrated by Fig. 7, 8 and 9. For the modern Earth, the albedo values obtained with the ISCCP data are higher than with Biome3.5, due to lower cloud cover with Biome3.5, leading to a lower VRE. This suggests that the Biome3.5 model probably overestimates the VRE. Nevertheless, relative comparisons between Biome3.5 results remain consistent, although the absolute values may be overestimated.

The main result from this study is that the climate differences between the Quaternary extrema and the modern Earth's climate have little impact on the vegetation signal, since the spectral signature of vegetation is not washed out during the LGM and does not increase very much during the Holocene optimum. There are nevertheless interesting differences in 'vegetation visibility' between these two extrema and the situation today, depending on the observer's position; when the northern hemisphere is mainly in view, vegetation is indeed more visible during the Holocene optimum as shown in Fig. 7 and Table 2. The VRE was typically 6%, thus higher than today (5%) or during the LGM (4%). This is mainly due to a greener Sahara as shown in Fig. 7(a). This is true for an observer with mostly the northern hemisphere in view, i.e., inclination $i = 45^\circ$. In inferior conjunction configuration, the crescent-shaped Earth mainly shows its northern part. There are no significant differences between modern and Holocene Earths (VRE $\approx 2\%$) and vegetation becomes almost undetectable for the Earth with the LGM large polar ice cap ($< 1\%$). If the observer is above the northern pole (observing from ecliptic North pole) with a half-illuminated Earth in view, there are again no significant differences between the modern and Holocene Earths (VRE $\approx 4\%$). However, as the North pole ice is much more extended during the LGM, the signal of the vegetation is significantly weaker (only 2%), due to the higher reflectance of a larger polar zone and the consequently smaller vegetated areas in view.

The three bottom lines from Table 2 give results for Earth views in which the southern hemisphere contribution is high, with inclination i ranging from 90 to 180° (Fig. 8 and 9). As pointed out in the Biome spectra section, our model probably overestimates the VRE values of scenes with the southern hemisphere mostly in view, as our calibration was made during fall time (May) in that hemisphere and deciduous species should have a lower VRE than with the spectra used in the simulation that have been collected in the northern hemisphere. Nevertheless, there are two trends to be mentioned: the first one is that the difference between the Holocene and modern period becomes negligible, because the Sahara contribution decreases or even vanishes from these southern view points. The second remark is that, paradoxically, the southern hemisphere VRE during the LGM is higher: this is induced by a greener Australia during the

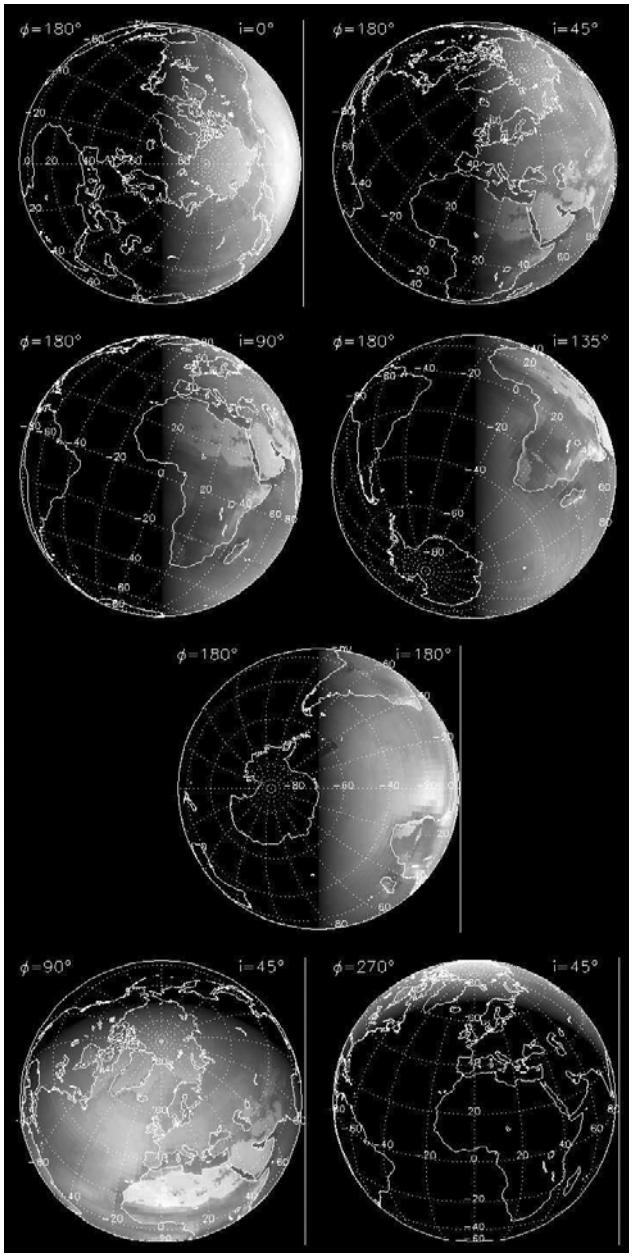

Fig. 9. Earth scenes reconstructed for the observer's positions given in Table 2, at 0° of central longitude. Scenes are for $\lambda = 750$ nm, a wavelength at which vegetation is brighter than in the visible. For a better readability, the radiance is shown here at power 0.7 to enhance the darker regions of the scene and underline the shape of the sunlit Earth seen by the observer.

https://doi.org/10.1017/S1473550409004406 Published online by Cambridge University Press

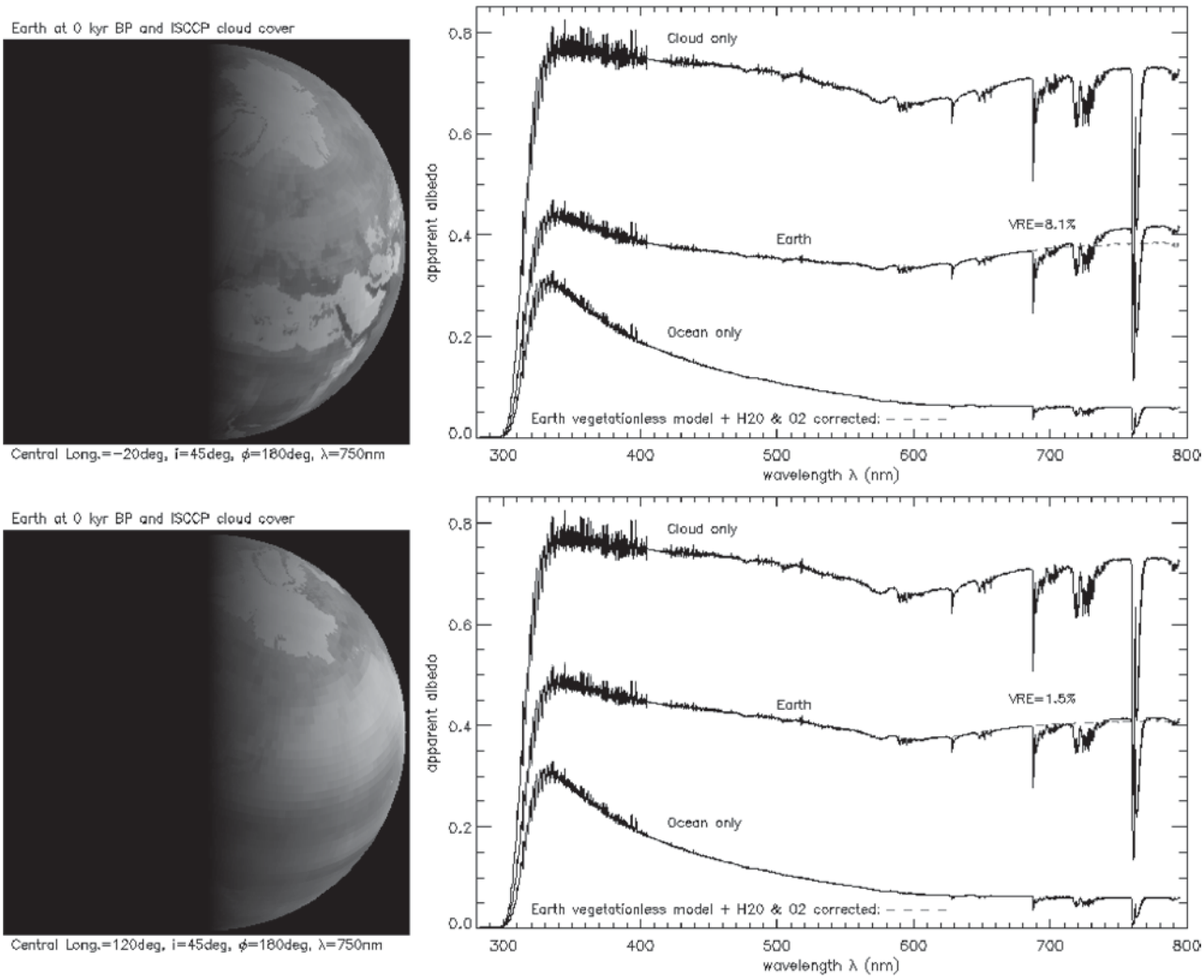

Fig. 10. Earth scenes and corresponding spectra reconstructed for two observer's positions at inclination $i=45^\circ$ (Table 7 and Fig. 7), for central longitudes of -20° (top, Africa and Europe in view) and 120° (bottom, Northern Pacific Ocean and Alaska in view) at which the model gives the maximum and minimum VRE, respectively. The Earth spectrum is in white, and a vegetationless model in dashed grey (moreover with O_2 and H_2O bands corrected), which allows one to visualize and calculate the VRE. For comparison, cloud and ocean spectra are shown. Scenes are for $\lambda=750$ nm, a wavelength at which vegetation is brighter than in the visible. For a better readability, the radiance is shown here at power 0.7 to enhance the darker regions of the scene and underline the shape of the sunlit Earth seen by the observer.

LGM, as we obtained a simulated wider distribution of temperate grassland and less desert in Australia using the Biome3.5 model (Fig. 3) at the Holocene optimum. As discussed above, this does not agree with observations of past vegetation and may arise from an incorrectly simulated climate over this region.

Figures 10 and 11 finally show modern Earth's scenes with corresponding spectrum obtained following the method described in the previous section. In Fig. 10, we show the spectrum for the central longitudes of -20° (Africa and Europe) and 120° (the Northern Pacific Ocean and Alaska) at which the model gives the maximum and minimum VRE, respectively of 8.1 and 1.5%. Fig. 10 shows the Earth spectra based on Biome3.5 data for central longitudes of -20° (Africa and Europe) at which the model gives the maximum VRE, i.e., 8.6, 11.0 and 6.3% at 0, 6 and 21 kyrBP, respectively.

Will the next space observatories be able to detect VRE-like features in an Earth-like planet spectrum? The Terrestrial Planet Finder Coronagraph mission (TPF-C) is aimed to make the direct detection and the characterization (multi-spectral imaging at a resolution of up to 70) of nearby terrestrial extrasolar planets in the visible range. The telescope would have an elliptical aperture of $(6 \text{ to } 8)\times 3.5\,\text{m}^2$ (Stapelfeldt *et al.* 2005; Shaklan *et al.* 2006). An Earth-like planet in the habitable zone is 10^{10} fainter than its parent star, making such planets very faint objects in the $V=28$ to 31 range. According to Stapelfeldt *et al.* (2005), exposure time of the order of one day will be needed to detect them and spectral characterization will add 'weeks of additional integration time per target'. More quantitatively, in a comparison of different types of coronagraphs (Guyon *et al.* 2006), the authors conclude that an Earth-like planet at about 10 pc

https://doi.org/10.1017/S1473550409004406 Published online by Cambridge University Press

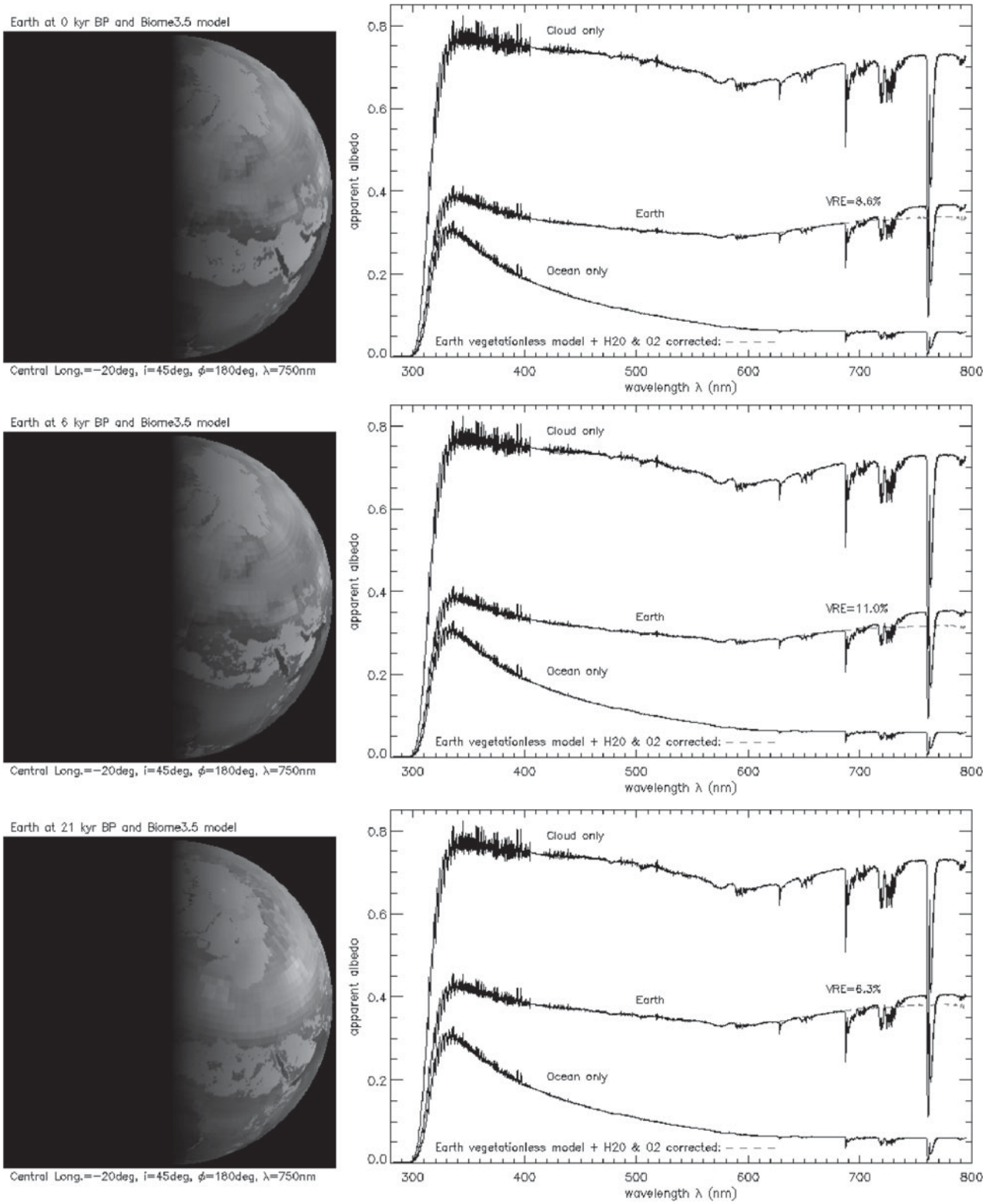

Fig. 11. Earth scenes and corresponding spectra reconstructed for one observer's position at inclination $i=45^\circ$ (Table 7 and Fig. 7), for central longitudes of -20° (Africa and Europe in view) at which the model gives the maximum VRE. The Earth spectrum is in white, and a vegetationless model in dashed grey (moreover with O_2 and H_2O bands corrected), which allows one to visualize and calculate the VRE. For comparison, cloud and ocean spectra are shown. Scenes are for $\lambda=750$ nm, a wavelength at which vegetation is brighter than in the visible. For a better readability, the radiance is shown here at power 0.7 to enhance the darker regions of the scene and underline the shape of the sunlit Earth seen by the observer.

https://doi.org/10.1017/S1473550409004406 Published online by Cambridge University Press

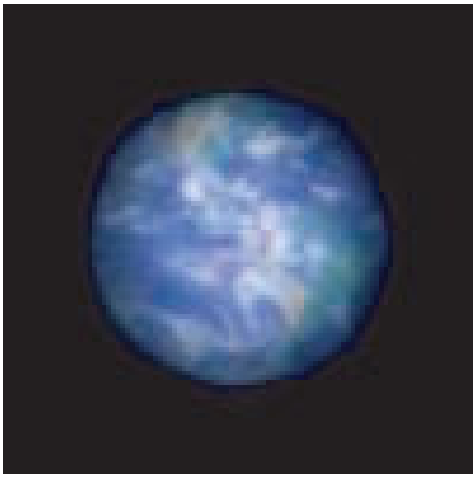

Fig. 12. Simulated image of the Earth at 3 pc (10 light-years) observed with a 150 km hypertelescope interferometric array made of 150 3 m mirrors working at visible wavelengths (from Labeyrie (1999)). North and South America are visible. Note that this simulation is done at visible wavelengths, while in the (very) NIR at 750 nm, vegetated areas would be much brighter and more easily detectable on continents. Spatial resolution at 750 nm would remain the same as at the visible wavelength with the same hypertelescope flotilla being spread over 225 km instead of 150 km.

could be detected in 2.3 hours with a signal-to-noise ratio of SNR = 7 with a 100 nm bandwidth from 0.5 to 0.6 μm with a 4 m telescope, and even in 14 minutes with a 6 m telescope, both equipped with one of the best performers of the comparison, a phase-induced amplitude apodization coronagraph. Now, if we want to be able to detect a 4% VRE-like feature in a spectrum at a resolution of 70 around 700 nm, the SNR should be about 80 for a 3 sigma detection, or 125 for a 5 sigma detection. With the 4 m coronagraphic telescope mentioned above, the total exposure time becomes very long, 18 and 44 weeks for 3 and 5 sigma detection, respectively. This is in agreement with the order of magnitude given by Stapelfeldt *et al.* (2005). With a 6 m telescope, the total exposure times decreases to 13 days and one month, respectively. If a telescope larger than the TPF-C-like telescopes mentioned above is considered, the exposure time will decrease again. According to Guyon *et al.* (2006), a planet could be detected in two minutes with a 12 m telescope. The total exposure times to detect a 4% feature in a spectrum would then decrease to 2 and 5 days, for 3 and 5 sigma detection, respectively. These very long exposure times suggest that features of a few percent will be extremely difficult to detect, maybe not even being within reach of a 'first-generation' 4 m TPF. A 6 m telescope seems to be the minimum to envisage the detection of seasonal variations. With exposure times of between 2 and 5 days, a 12 m telescope would probably not freeze the rotation of the planet and, rather, give an integrated spectrum of the planet over several rotations, but atmospheric changes at time scales of the order of a week or longer would be possible to detect and follow up, as well as longer seasonal variations.

Unfortunately TPF-C might not fly before 2025, and in the meantime, a smaller instrument could look for bigger and closer terrestrial planets: A 2 m class space coronagraph, such as SEE-COAST, could indeed detect a VRE on super-Earths closer than 3–6 pc (Schneider *et al.* 2008), depending on their radius, the maximum value of which is presently unclear. These super-Earths are as habitable as Earth-sized planets.

More ambitious instruments that might fly later this century will allow us to make a step furthermore in the characterization of these planets and the observation of 'exo-vegetation'. Hypertelescopes in space – interferometric sparse arrays of small telescopes – will indeed allow us to see Earth-like planets as *small resolved disks* several resolution elements (resels) across (Labeyrie 1999; Labeyrie *et al.* 2008) and this clearly will help us to detect photosynthetic life on these planets. For example, a 150 km hypertelescope would provide 40 resels across an Earth at 3 pc in yellow light (Labeyrie 1999) and a formation of 150 3 m mirrors would collect enough photons in 30 minutes to freeze the rotation of the planet and produce an image with at least ≈300 resels, and up to thousands depending on array geometry (Fig. 12). At this level of spatial resolution, it will be possible to identify clouds, oceans and continents, either barren or perhaps (hopefully) conquered by vegetation.

Conclusion

In order to mimic an Earth-like extrasolar planet observed without spatial resolution, i.e., as a single dot, in a different climate state than our contemporary Earth, we considered the Earth during the last climatic extrema, 6 and 21 kyr ago, and studied the vegetation spectral signature integrated over the full illuminated phase seen by the observer. The results presented in this paper suggest that the vegetation disk-averaged signature remained visible in Earth's spectra during these climatic extrema, with VRE values close to those for the modern Earth. This is encouraging for the future space missions that will characterise Earth-like extrasolar planets and look for biosignatures. Our discussion emphasized some differences induced, for example by the greener Sahara during the Holocene optimum, or by the large northern ice cap during the LGM. Results would probably benefit in accuracy from radiative transfer calculations, an implementation of the sun glint effect and the BRDFs of all scattering surfaces being included in the model. The spectra would thence also display a more accurate Rayleigh scattering 'slope' and absorption bands depth. Further, improved GCM estimates for these past periods are now available, including coupled ocean–atmosphere simulations (Braconnot *et al.* 2007), as well as dynamic vegetation models (Sitch *et al.* 2003), both of which may help improve the past vegetation distributions obtained here. All of these improvements could be considered for future developments.

Of course, a next step in this work could also be the consideration of the Earth at much older epochs, when continents had a very different shape than today and climates

https://doi.org/10.1017/S1473550409004406 Published online by Cambridge University Press

were maybe much more extreme than those considered in this work, although paleoclimatic models are probably less confident for these epochs. Nevertheless, it would probably provide us with relevant illustrations of Earth spectrum variability over one full day, and related VRE variations. Current climate change, thence biome maps for the end of this century, might also tell us if vegetation will remain a detectable biomarker for observers out there.

Acknowledgements

This work was supported in part by the French CNRS *GdR Exobiologie*. The authors thank Jean-Claude Lebrun (Service d'Aéronomie, CNRS, Verrières-le-Buisson, France) who provided the MODTRAN spectra of H_2O and O_2, and Andreas Richter (Institute of Environmental Physics, University of Bremen, Germany) for SCIATRAN data and discussions on Rayleigh scattering.

References

Arnold, L. (2008). *Space Sci. Rev.* **135(1–4)**, 323–333 (DOI:10.1007/s11214-007-9281-4), also in *Strategies of Life Detection*, Space Sciences Series ISSI 2008, eds Botta, O., Bada, J.L., Gomez-Elvira, J., Javaux, E., Selsis, F., Summons, R., Springer, Berlin (DOI:10.1007/978-0-387-77516-6_1).

Arnold, L., Bréon, F.-M., Brewer, S., Guiot, J., Jacquemoud, S. & Schneider, J. (2003). The green vegetation as a biosignature on Earth and Earth-like planets: POLDER data and Earthshine observations. In *Proc. Conf. SF2A-2003: Scientific Highlights 2003*, eds Combes, F., Barret, D., Contini, T. & Pagani, L., Bordeaux, France, 16–20 June, 2003, pp. 133–136. EDP-Sciences, Les Ulis.

Arnold, L., Gillet, S., Lardière, O., Riaud, P. & Schneider, J. (2002). *Astron. Astrophys.* **392(1)**, 231–237.

Bonfils, C., Noblet-Ducoudré, N., Braconnot, P. & Joussaume, S. (2001). *J. Clim.* **14(17)**, 3724–3737.

Braconnot, P. *et al.* (2007). *Clim. Past* **3**, 261–277.

Bréon, F.-M. & Henriot, N. (2006). *J. Geophys. Res.* **111**, C06005, doi:10.1029/2005JC003343.

Clark, R.N. (1999). Chapter 1: spectroscopy of rocks and minerals, and principles of spectroscopy. In *Manual of Remote Sensing*, Vol. 3, Remote Sensing for the Earth Sciences, ed. Rencz, A.N., pp. 3–58. John Wiley and Sons, New York.

Claussen, M., Kubatzki, C., Brovkin, V., Ganopolski, A., Hoelzmann, P. & Pachur, H.J. (1999). *Geophys. Res. Letters* **24(14)**, 2037–2040.

Fairbanks, R.G. (1989). *Nature* **342**, 637–642.

Guyon, O., Pluzhnik, E.A., Kuchner, M.J., Collins, B. & Ridgway, S.T. (2006). *Astrophys. J. Supp. Series* **167(1)**, 81–99.

Hamdani, S., Arnold, L., Foellmi, C., Berthier, J., Billeres, M., Briot, D., François, P., Riaud, P. & Schneider, J. (2006). *Astron. Astrophys.* **460**, 617–624.

Haxeltine, A. & Prentice, I.C. (1996). *Global Biogeochem. Cycles* **10(4)**, 693–709.

Hewitt, C.D. & Mitchell, J.F.B. (1996). *J. Clim.* **9**, 3505–3529.

Hewitt, C.D. & Mitchell, J.F.B. (1997). *Clim. Dynam.* **13**, 821–834.

Labeyrie, A. (1999). *Science* **285(5435)**, 1864–1865.

Labeyrie, A., Le Coroller, H., Dejonghe, J., Lardière, O., Aime, C., Dohlen, K., Mourard, D., Lyon, R. & Carpenter, G.K. (2008). *Exper. Astron.* in press (DOI:10.1007/s10686-008-9123-8).

Leemans, R. & Cramer, W. (1991). *The IIASA Climate Database for Mean Monthly Values of Temperature, Precipitation & Cloudiness on a Terrestrial Grid.* International Institute for Applied Systems Analysis, Laxenburg, Germany.

Léna, P., Lebrun, F. & Mignard, F. (1996). *Méthodes physiques de l'observation*, 2nd edn, pp. 55. CNRS Editions, EDP Sciences, Paris.

Manabe, S. & Strickler, R.F. (1964). *J. Atmos. Sci.* **21**, 361–385.

Prentice, I.C., Jolly, D. & BIOME 6000 Participants (2000). *J. Biogeogr.* **27**, 507–519.

Qiu, J. *et al.* (2003). *J. Geophys. Res.* **108(D22)**, ACL 12-1.

Ritchie, J.C. & Haynes, C.V. (1987). *Nature* **330**, 645–647.

Schneider, J. *et al.* (2008). *Exper. Astron.*, in press (DOI:10.1007/s10686-008-9129-2).

Shaklan, S.B., Balasubramanian, K., Ceperly, D., Green, J.J., Hoppe, D.J., Lay, O.P., Lisman, P.D. & Mouroulis, P.Z. (2006). Terrestrial Planet Finder Coronagraph Instrument Design. In *Direct Imaging of Exoplanets: Science & Techniques, Proc. of the IAU Colloquium #200*, eds Aime, C. & Vakili, F., pp. 577–580. Cambridge University Press, Cambridge.

Sitch, S. *et al.* (2003). *Global Change Biol.* **9**, 161–185.

Stapelfeldt, K., Beichmann, C. & Kuchner, M. (2005). *New Astron. Rev.* **49**, 396–399.

Woolf, N.J., Smith, P.S., Traub, W.A. & Jucks, K.W. (2002). *Astrophys. J.* **574**, 430–433.